A highly stable host with ultralow strain in a layered Fe/Mn-based cathode for advanced Sodium-ion Batteries

Rui Qi[a,1], Mihai Chu[a,1], Wenguang Zhao[a], Ziwei Chen[a], Lei Liao[b], Shisheng Zheng[a], Lei Xie[c], Tongchao Liu[d], Yang Ren[e], Lei Jin[f], Khalil Amine[d,g], Feng Pan[a,] and Yinguo Xiao[a,*]*

[a] School of Advanced Materials, Peking University, Shenzhen Graduate School, Shenzhen, 518055, China

[b] Beijing National Laboratory for Condensed Matter Physics, Institute of Physics, Chinese Academy of Sciences, 100190 Beijing, China

[c] Institute of Nuclear Physics and Chemistry, China Academy of Engineering Physics, Mianyang, 621900, China

[d] Chemical Sciences and Engineering Division, Argonne National Laboratory, Lemont, IL 60439, USA

[e] X-ray Science Division, Argonne National Laboratory, Lemont, IL 60439, USA

[f] Ernst Ruska-Centre for Microscopy and Spectroscopy with Electrons, Forschungszentrum Jülich GmbH, 52425 Jülich, Germany

[g] Material Science and Engineering, Stanford University, Stanford, CA 94305, USA

Author Information

[1] These authors contributed equally to this work.

* Corresponding author: panfeng@pkusz.edu.cn (F. Pan), y.xiao@pku.edu.cn (Y. Xiao)

Abstract

Sodium-ion batteries (SIBs) with iron- and manganese-based cathode electrodes have exhibited great promise in the grid-scale energy storage systems, on the basis of the satisfactory theoretical capacity, as well as huge abundance, low price and non-toxicity of raw materials. However, the inferior cycle life of cathode materials originating from their poor structural stability remains a formidable challenge towards practical applications. Here, an efficient strategy of improving the structure durability is demonstrated in iron- and manganese-based cathodes by dual heteroatom doping. The as-obtained P2-type $Na_{0.65}Li_{0.08}Cu_{0.08}Fe_{0.24}Mn_{0.6}O_2$ cathode delivers superior cyclability (88.2% capacity retention for 500 cycles at 2C), fabulous rate capability (76% capacity retention at 5C compared to 0.1C), and a useable reversible capacity of around 85 mAh g^{-1} at 0.1C. Through in-depth characterizations, the underlying structure-property relationship is established, revealing that the complete solid-solution reaction during cycling ensures the ultralow volume variation and excellent electrochemical performance. These results highlight the significance of fabricating a stable host for the design and development of advanced SIBs with long life.

Keywords: sodium-ion battery, Fe- and Mn-based layered oxide cathodes; co-substitution strategy, solid-solution reaction, lattice strain

1. Introduction

Owing to the ever-growing demands for environmentally-benign energy solutions, research and development of large-scale electrical energy storage systems (EESs) for the integration of intermittent renewable energy sources, such as solar, wind and geothermal, is becoming increasingly imperative [1, 2]. In this regard, rechargeable sodium-ion battery (SIB) is considered as one of the most attractive options for grid-scale EESs and an alternative to lithium-ion batteries due to the highly abundant and wide distribution of sodium resources compared to lithium [3]. Among the various cathode materials for SIBs, the layered transition-metal oxides (Na_xTMO_2, $0<x\leq1$, TM=Ni, Co, Mn, Fe, V, etc.) have been regarded as one of the most promising candidates for several advantages in terms of their facile synthesis and 2D Na^+ diffusion pathway [4].

In general, Na_xTMO_2 can be classified into two major groups according to the oxygen stacking sequence and local environment of Na^+, namely P2-type (P: prismatic) and O3-type (O: octahedral) [5]. P2-phase oxides normally exhibit fewer phase transitions and better rate capability in comparison with the corresponding O3-type counterpart on account of their larger prismatic sites and direct diffusion pathways for Na^+ [6]. As a consequence, P2-$Na_{2/3}Fe_{1/2}Mn_{1/2}O_2$ possesses a much more remarkable electrochemical performance than O3-

$NaFe_{1/2}Mn_{1/2}O_2$, delivering a high capacity of 190 $mAh \cdot g^{-1}$ within the voltage of 1.5V-4.3V [7]. It is also worth noting that both iron and manganese elements are extremely abundant in the earth's crust among all the 3d transition metals [8]. The P2 Na-Fe-Mn-O cathodes obviously demonstrate great potential as commercialized cathodes for SIBs in view of their satisfactory theoretical capacity, low cost in raw materials and environmental benignity [8-11]. However, the practical application of these P2-type Fe- and Mn- based oxides is seriously hindered by their insufficient structural stability during cycling, which is ascribed to the formation of unfavorable P2-Z phase transition at a high-voltage region and the destabilization of the crystal structure associated with Jahn-Teller distortion of Mn^{3+} upon Na^+ (de)intercalation [12-14]. In addition, P2-type $Na_xFe_{1-y}Mn_yO_2$ materials are hygroscopic, thus resulting in a shorter lifetime and added cost for storage and transportation [15].

To alleviate the aforementioned issues faced by P2-$Na_xFe_{1-y}Mn_yO_2$, tremendous efforts have been exerted in previous studies, such as heteroatom doping [8, 11], surface engineering [16] and nanoscale design [17]. Noticeably, doping various metallic cations (inactive ions: Li^+ [18, 19], Mg^{2+} [20], Al^{3+} [21], Ti^{4+} [22, 23]; active ions: Ni^{2+} [24], Co^{3+} [25, 26], Cu^{2+} [27, 28]) is commonly recognized to be an effective way to improve their performance. For example, Ni and Co were introduced to transition metal layers to fabricate the trinary Ni/Fe/Mn- and Co/Fe/Mn-based oxides respectively, showing an improved performance to some extent by relieving the phase transition and structural distortion [25, 29]. Considering the relatively expensive price of Ni and Co, a Cu-substituted P2-$Na_{7/9}Cu_{2/9}Fe_{1/9}Mn_{2/3}O_2$ was synthesized. This material exhibited a reversible capacity of 89 $mAh \cdot g^{-1}$ at 0.1C and a complete solid-solution reaction with good capacity retention (85% after 150 cycles at 1C) [30]. Nonetheless, it is still not competent to achieve ultra-long-term cycles in P2-type Fe- and Mn- based cathodes. It should be demonstrated that for grid-scale EESs, low production cost and superior cycling stability are critically important [31]. Besides, for P2-type Fe- and Mn- based oxides, impurities are inclined to produce without suitable compositions and substituents/dopants [32]. Therefore, it is urgent to explore novel Ni/Co free cathodes with excellent calendar life and high tolerance toward moisture through a scalable route.

Herein, Li/Cu co-substitution is proposed to improve the practicality of P2-$Na_xFe_{1-y}Mn_yO_2$, since dual heteroatom doping strategy could not only combine different merits of dopants but boost the concentration of heteroatoms in materials [33]. For example, some quaternary, quinary and even high entropy layered oxide cathodes enabled by doping two or more metallic elements commonly delivered good energy storage properties [34-36]. Nevertheless, to the best of our knowledge, the heteroatom co-doping method has rarely been adopted for the P2-type Fe- and Mn- based system. Among all of the dopant cations, Li substitution in the TM layer is considered

as structure stabilizer because the monovalent Li^+ is beneficial to keep more Na^+ retain in the deeply desodiated structure to maintain electrostatic equilibrium [37]. Consequently, suppressed phase transitions (i.e., P2-O2, P3-P'3) and smooth charge-discharge curves were reported in Li-substituted Na_xTMO_2 cathodes [38-40]. Meanwhile, the Cu-doped oxides were developed, including P2-$Na_{0.67}Cu_{0.33}Mn_{0.67}O_2$ [41], P2@P3 $Na_{0.78}Cu_{0.27}Zn_{0.06}Mn_{0.67}O_2$ [42], etc., in which the reversible Cu^{2+}/Cu^{3+} redox is responsible for the improved working potential and air stability.

Enlighted by the above considerations, a quaternary P2-type $Na_{0.65}Li_{0.08}Cu_{0.08}Fe_{0.24}Mn_{0.6}O_2$ (NLCFM) was successfully designed for the first time via Li/Cu co-substitution. As a comparison, the electrochemical performance of undoped P2-$Na_{0.65}Fe_{0.4}Mn_{0.6}O_2$ (NFM), mono-doped P2-$Na_{0.65}Li_{0.08}Fe_{0.32}Mn_{0.6}O_2$ (NLFM) and P2-$Na_{0.65}Cu_{0.08}Fe_{0.32}Mn_{0.6}O_2$ (NCFM) were systematically investigated, and their phase structures were confirmed by neutron diffraction coupled with X-ray diffraction. For the P2-NLCFM electrode, in-situ synchrotron high-energy X-ray diffraction (HEXRD) reveals that the unwanted P2-Z phase transition has been strongly mitigated during the charge/discharge process with the unit cell volume variation as small as about 0.7%. As a consequence, outstanding structural stability and greatly enhanced rate capability were achieved. The Li/Cu co-doping NLCFM cathode exhibits a specific capacity of around 85 $mAh \cdot g^{-1}$ at 0.1 C between 2.5-4.2V with a high average voltage of 3.5V and ultra-stable cycle performance (88.2% capacity retention at 2C after 500 cycles). The ex-situ XRD experiments, high-resolution transmission microscopy (HRTEM), galvanostatic intermittent titration technique (GITT) and differential electrochemical mass spectrometry (DEMS) were further conducted to investigate the linkage between electrochemical performance and structure durability, and demonstrated the significance of a stable host for Na^+ insertion/extraction.

2. Experimental Section

2.1. Materials Synthesis

$Na_{0.65}Fe_{0.4}Mn_{0.6}O_2$ (NFM), $Na_{0.65}Li_{0.08}Fe_{0.32}Mn_{0.6}O_2$ (NLFM), $Na_{0.65}Cu_{0.08}Fe_{0.32}Mn_{0.6}O_2$ (NCFM) and $Na_{0.65}Li_{0.08}Cu_{0.08}Fe_{0.24}Mn_{0.6}O_2$ (NLCFM) were prepared by a conventional solid-state reaction from the precursor of Na_2CO_3 (Sinopharm Chemical, 99.8%), Fe_2O_3 (Aladdin, 99.9%), Li_2CO_3 (Sinopharm Chemical, 99.99%), CuO (Sinopharm Chemical, 99%), and Mn_2O_3 (98%, Sinopharm Chemical). For $Na_{0.65}Fe_{0.4}Mn_{0.6}O_2$, Na_2CO_3, Fe_2O_3, and Mn_2O_3 were mixed together with a molar ratio of 0.67:0.4:0.6 (3% excess Na_2CO_3 to compensate for the volatilization loss at high temperatures) and thoroughly ground by a ball mill at 400r min^{-1} for 6h. The resulting mixture was pressed into pellets under the pressure of 20Mpa. Then, the pellets were calcined at 900°C for 15 h in O_2. After cooling down naturally, the sample was transferred to an Ar-filled glovebox immediately until use. The synthesis procedure of doped samples,

NLCFM, NLFM and NCFM followed the identical procedure via mixing the relevant oxide in a stoichiometric ratio.

2.2. Materials Characterizations

The composition of the final materials was detected by inductively coupled plasma-atomic emission spectrometry (ICP-AES, JY2000-2, HORIBA JOBINYVON). The crystalline structures of the samples were investigated by both X-ray and neutron diffraction measurements. The X-ray diffraction (XRD) patterns were collected on a Bruker D8 Discover diffractometer with Cu Kα radiation of λ = 1.5405(6) Å within the 2θ range of 10-80°. Neutron powder diffraction (NPD) experiments were performed at room temperature on the High-Pressure Neutron Diffractometer (HPND) at China Mianyang Research Reactor (CMRR). Room-temperature data were collected at a wavelength of λ = 1.5907(0) Å. Rietveld refinement of the diffraction profiles was carried out using the FullProf package suite. In addition, the particle morphology was examined using a scanning electron microscope (SEM, ZEISS SUPRA-55) with an Energy Dispersive Spectroscopy (EDS, OXFORD, X-MaxN TSR). High-resolution transmission electron microscopy (HRTEM) images were obtained on a JEOL-3200FS field-emission transmission electron microscopy (FETEM) with 300 kV accelerating voltage. To observe the oxidation states of the transition metal elements, electron energy loss spectroscopy (EELS) data were collected using a 300KV aberration-collected STEM (JEM-ARM300F, JEOL Ltd). X-ray photoelectron spectra (XPS) was performed by a Thermo Fisher ESCALAB 250X using a monochromatic Al Kα X-ray source, and all the binding energy were calibrated with C 1s signal at 284.8 eV. Especially for the ex-situ EELS, XPS and XRD measurements, the post cycled electrodes were first transferred to a hermetically sealed transfer chamber in a glovebox filling with Ar to prevent exposure to air or moisture. As for in-situ XRD studies, the time-resolved HEXRD experiment was performed on NLCFM material during the first cycling at beamline 11-ID-C, Advanced Photon Source (APS), Argonne National Laboratory (ANL), with the wavelength of 0.1173 Å. The NLCFM cathode electrode was prepared using PVDF as binder on an ultrathin Al foil and the diffraction patterns were collected every 10 min in a 2θ range of 0°-4° under cycling. Moreover, DEMS experiments were carried out in a customized cell connected to a gas flow controller and mass spectrometer by using Agilent Technologies 5975C.

2.3. Electrochemical Measurements

The cathode electrodes were prepared by using the following steps. As-prepared active materials were mixed with acetylene black and poly (vinylidene fluoride) (PVDF) with a weight ratio of 8:1:1 in N-methyl-2-pyrrolidone (NMP). After stirring for 6h, the homogeneous slurry

was spread on the clean Al foil, followed by drying at 110℃ in a vacuum oven overnight. Metallic Sodium disk was employed as the counter electrode and glass fiber was used as the separator. The electrolyte was a solution of 1M $NaClO_4$ in ethylene carbonate/diethyl carbonate (EC/DEC,1:1 in volume) with fluoroethylene carbonate (FEC 5% in volume) as additive. The assembly of the CR2032-type coin cells was carried out in an Ar-filled glove box. Galvanostatic discharge/charge tests were performed using a NEWARE battery cycler at room temperature. In the ultra-long cycling test, one formation cycle was performed at 0.1 C, followed by cycling at 2 C. GITT measurement was carried out on a Maccor test cabinet in the voltage range of 2.5-4.2V vs Na^+/Na. The Cyclic voltammogram curves were tested by the CHI660D electrochemical workstation (CHI Instruments, China).

3. Results and discussion

3.1. Structure and chemical composition analysis

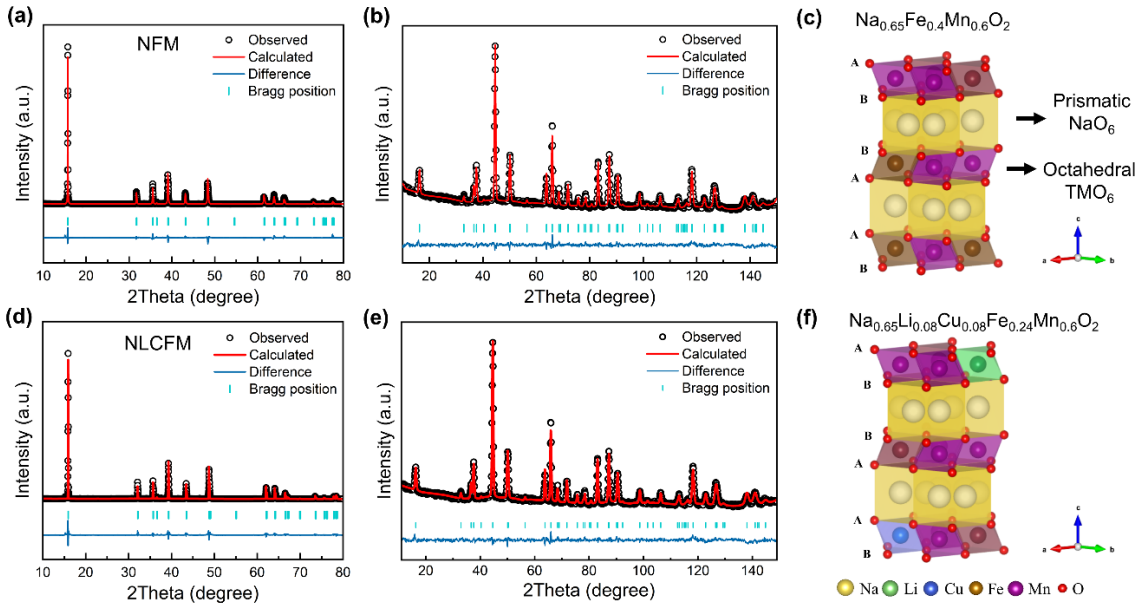

Fig. 1. Crystal structure characterization on powder samples of NFM and NLCFM. (a-b, d-e) Observed and calculated XRD and NPD profiles for NFM and NLCFM: (black) observed; (red) calculated; (blue) difference plot; (green bars) Bragg reflections. (c, f) Schematic illustration of the crystal structure of NFM and NLCFM.

To prove the effectiveness of the Li/Cu co-substitution, the target samples NFM and NLCFM, as well as mono-doped samples, were synthesized by a solid-state method. ICP-AES measurement results indicate that the chemical formulas of as-prepared materials are consistent with the expected stoichiometry (Table S1). To obtain the accurate lattice parameters and precise atomic positions, the joint refinements based on both XRD and NPD profiles were performed. As X-ray alone is not sensitive to light elements such as Li and could hardly distinguish elements

with similar atomic numbers such as Fe and Mn, neutron could make up for that with the advantage of the sensitivity against nuclei of all atoms involved. As shown in Fig.1 and Fig. S1, the Rietveld refined NPD and XRD patterns demonstrate that all Bragg reflections in each individual sample, as expected, could be assigned to the P2-type layered structure (space group: P63/mmc, JCPDF no. 27–751) without any impurity. The good agreement between the fitting and experiment patterns confirms that Li, Cu, Fe and Mn atoms are all located in the TM layer (Fig. 1c and f). Additionally, there is no noticeable reflection corresponding to long-range in-plane ordering associated with TM ion units or Na^+/vacancy ordering. The detailed structural information is given in Table S2. A slight lattice contraction was observed with the introduction of Li and Cu, where a = 2.92237 Å and c =11.23362 Å for NFM and a = 2.90274 Å and c = 11.146932 Å for NLCFM. This contraction was caused by the oxidation of the Mn^{3+} to Mn^{4+} (ionic radii of Mn^{3+} is larger than that of Mn^{4+}) due to the presence of the Li^+ and Cu^{2+} in the TM layer. In addition, after co-doping, the thickness of Na layer (T_{Na}) decreases while the thickness of TM layers (T_{TM}) increases.

The HRTEM images in Fig. S2 further corroborate the typical P2 structure of all four samples, where the (002) plane and the fast Fourier transform (FFT) images (inset of Fig. S2) are clearly shown. However, for the samples containing the single dopant element, when their anticipated content of heteroatom was raised to the same amount in NLCFM ($Na_{0.65}Li_{0.08}Cu_{0.08}Fe_{0.24}Mn_{0.6}O_2$), the expected stoichiometry ($Na_{0.65}Li_{0.16}Fe_{0.24}Mn_{0.6}O_{2-x}$, $Na_{0.65}Cu_{0.16}Fe_{0.24}Mn_{0.6}O_2$) could not be achieved and the impurities would arise (Fig. S3), implying the co-substitution strategy is beneficial to boost the content of heteroatoms in materials [33]. In addition, SEM images show that all samples exhibit plate-like particles with around 2~4μm in size (Fig. S4). EDS mapping images reveal that various elements uniformly distribute throughout particles without any aggregation (Fig. S5). All the above results confirm the target cathodes are successfully prepared and the heteroatom-doping strategy has negligible influence on sample morphology and element distribution, laying the groundwork for further investigating their performance and behaviors.

3.2. Electrochemical behavior

The electrochemical performances of the NFM and NLCFM were comparatively studied in sodium half cells. Fig. 2a and 2b show the galvanostatic charge/discharge curves in a voltage range of 2.5–4.2 V at a current rate of 0.1 C (10 mA g^{-1}). In the first cycle, NFM electrode delivers a discharge specific capacity of 100 mA h g^{-1} and two distinct voltage plateaus at 4.1V and 3.5 V are observed, corresponding to phase transitions [14]. A much lower discharge capacity of 85 mA h g^{-1} is left just after 10 cycles accompanied by the shortening of the voltage

plateaus, in accordance with the rapid decay of two obvious peaks in the dQ/dV curves (Fig. 2d), revealing that severe irreversible behaviors occur during the cycling. In contrast, NLCFM electrode proceeds through a more solid-solution like reaction (Fig. 2b), as reflected in sloping charge/discharge profiles as well as highly reversible dQ/dV curves (Fig. 2e). Interestingly, the specific capacity of NLCFM gradually increases from 78 mA h g^{-1} to 85 mA h g^{-1} during the initial 10 cycles, and even reaches 90 mA h g^{-1} after 40 cycles (Fig. 2c), which could be attributed to the minimization of Mn^{3+} content after Li/Cu co-substitution and consequent gradual electrochemical activation of Mn^{4+} component. Their performance differences are clearly demonstrated in Fig. 2c. With the increasing cycle number at 0.1C, the NFM electrode encounters very fast capacity decay with an inferior retention of only 40% after 100 cycles, while NLCFM exhibits great superiority in both cyclability and average potential. Moreover, the GITT result in Fig. 2f and S6 indicates that Na-diffusion coefficients (D_{Na^+}) in NFM exhibits a sharp drop at around 3.5V during the initial discharging, corresponding well to the plateau shown in discharge profile (Fig. 2a). The occurrence of minima signals the attenuation of Na^+ mobility, which could be attributed to the host rearrangement [43]. All these results preliminarily demonstrate the feasibility and effectiveness of our heteroatom co-doping strategy, in which the introduction of Li/Cu as heteroatoms is greatly in favor of the cycling performance, midpoint voltage and rate capability of cathodes.

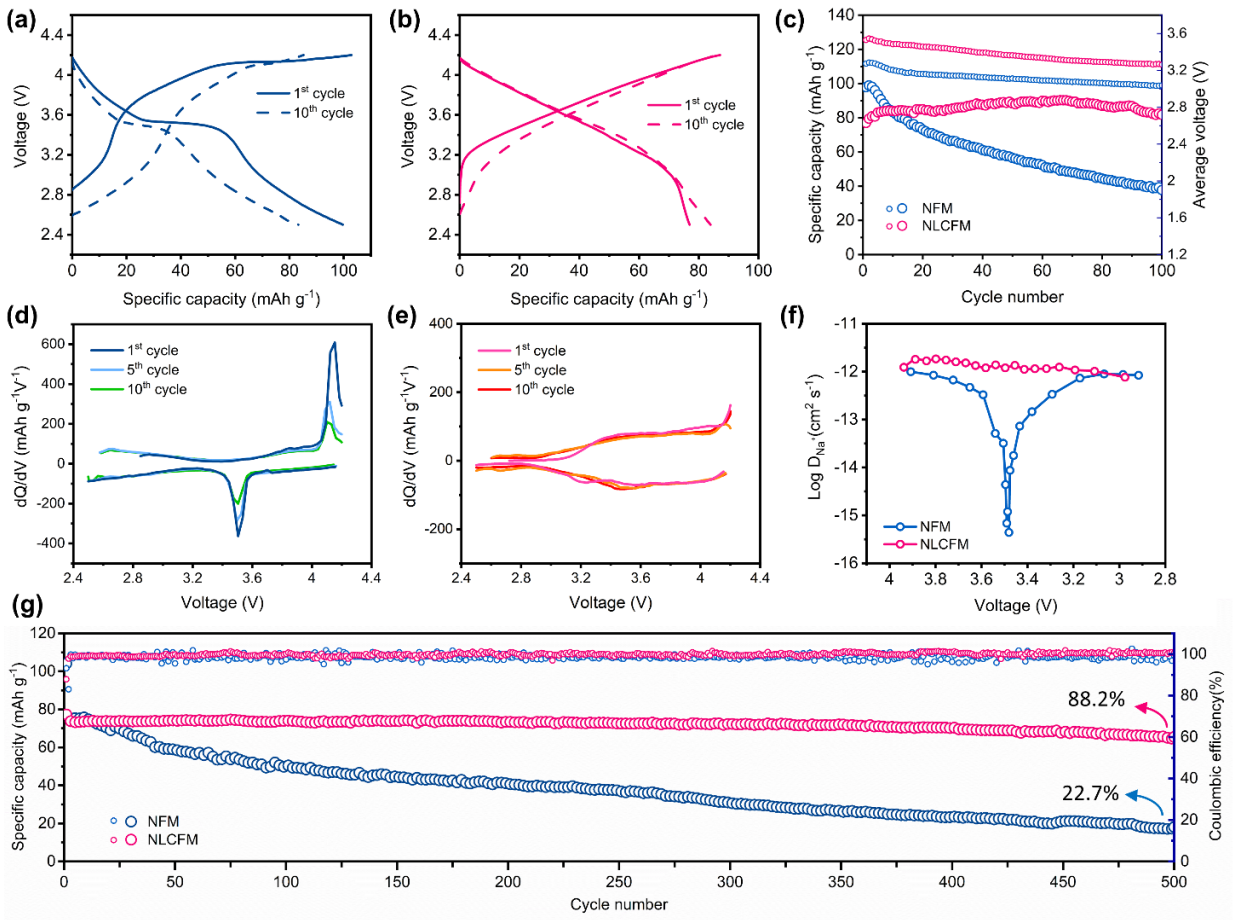

Fig. 2. Electrochemical performance of NFM and NLCFM electrodes in half-cell system. (a-b) Galvanostatic charge/discharge curves at 0.1C of NFM and NLCFM electrodes, respectively. (c) Comparisons of average voltage and cycling performance at 0.1C. (d-e) dQ/dV curves of NFM and NLCFM electrodes. (f) Na^+ chemical diffusion coefficient calculated from GITT data for NFM and NLCFM electrodes. (g) Cycling performance of NFM and NLCFM at 2C over 500 cycles.

In order to clarify the role of each heteroatom in the co-substitution NLCFM sample, four as-prepared electrodes including mono-doped ones were tested by CV between 2.5 and 4.2 V, shown in Fig. S7. In pristine electrode, the anodic peaks at potentials higher than 3.9 V, as well as the cathodic peak at around 3.5 V, are attributed to the redox reactions of the Fe^{3+}/Fe^{4+} couple, while the peaks below 2.7 V should correspond to the redox reactions of the Mn^{3+}/Mn^{4+} [24]. With the Cu-substitution, the abovementioned anodic peak of Fe^{3+}/Fe^{4+} becomes broader due to the incorporation of oxidation/reduction peaks of Cu^{2+}/Cu^{3+} (4.0/3.9 V) [28], which could contribute to the capacity and improve the working potential in the electrode. With the Li-substitution, the smoothing of peaks in NLFM are achieved and the CV profiles in the first 5 cycles have better overlapping compared to the NFM and NCFM, suggesting optimized

structural reversibility during cycling. In the case of Li/Cu co-substitution, the disappearance of Mn^{3+}/Mn^{4+} redox peaks induced by maximization of Mn^{4+} content, and the mergence of Fe^{3+}/Fe^{4+} and Cu^{2+}/Cu^{3+} redox peaks [28, 30], jointly lead to more sloping and flat CV curves, indicating that the structure of NLCFM is stable upon Na^+ insertion/extraction. In addition, as elucidated in Fig. S8 and Fig. S9, these redox activities are detected by XPS and EELS. Given the results of the rate and cycling performance of these four electrodes in Fig. S10, it further confirms that Cu contributes to the capacity and Li improves the stability. With the help of these two kinds of heteroatom substitution, the NLCFM exhibits the best rate capability and cycling stability among four kinds of Fe- and Mn- based oxides. Therefore, a longer cycling test of NLCFM was conducted at 2 C and it exhibits outstanding cycling performance, as shown in Fig. 2g. A capacity retention of 88.2% is achieved after 500 cycles, with the capacity loss rate of only about 0.026% per cycle, corroborating the superior reversibility during cycling.

3.3. Structural evolution of electrodes upon Na^+ (de)intercalation

To understand the nature of discrepancies in electrochemical performance, the structural evolutions of the NFM and NLCFM electrodes during the first cycle were analyzed by ex-situ XRD (Fig. 3). Seven key points indicated by colored circles were selected, and corresponding XRD patterns of NFM are shown in Fig. 3a. It is clear that the phase transformation occurs when the NFM electrode crosses the long plateau at around 4.1V and 3.5V, respectively, in accordance with the low D_{Na}^+ deduced from GITT results. When the NFM electrode is charged to 4.1 V, the intensity of P2 (002) peak at $2\theta = 15.8°$ decreases dramatically along with the emergence of a new characteristic peak at its right side. Combined with other reflections, this newly formed phase is assigned to the "Z" phase with low crystallinity [7, 12]. Upon further charging, this new characteristic reflection gradually reached $2\theta = 17.1°$ and the "Z" phase almost dominated the structure. The peaks indexed in "Z" phase are weak and broad, indicating an evolving intergrowth between the P-type stacking (Na in prismatic sites) and O-type stacking (Na in octahedral sites) [44]. During the discharge process, the P2 reflections reappear at around 3.5V at the expense of the "Z" phase. The evolution of the lattice parameters determined by Le Bail fitting methods could also demonstrate the phase transition. As presented in Fig. 3b, the in-plane lattice parameter experiences an evident decrease from 2.91 Å to 2.85 Å upon desodiation process. Meanwhile, the average interlayer distance of NFM undergoes a sharp contraction from 5.63 Å to 5.20 Å because the interlayer spacing of newly formed O-type layers induced by the glide of TMO_2 slabs at high voltage is much smaller than the original P-type layers [45], as illustrated in Fig. S11. Although all these lattice parameters nearly return to their initial values at the end of discharge, suggesting a reversible P2-Z phase transition, the huge lattice variations were still clearly observed in the NFM electrode.

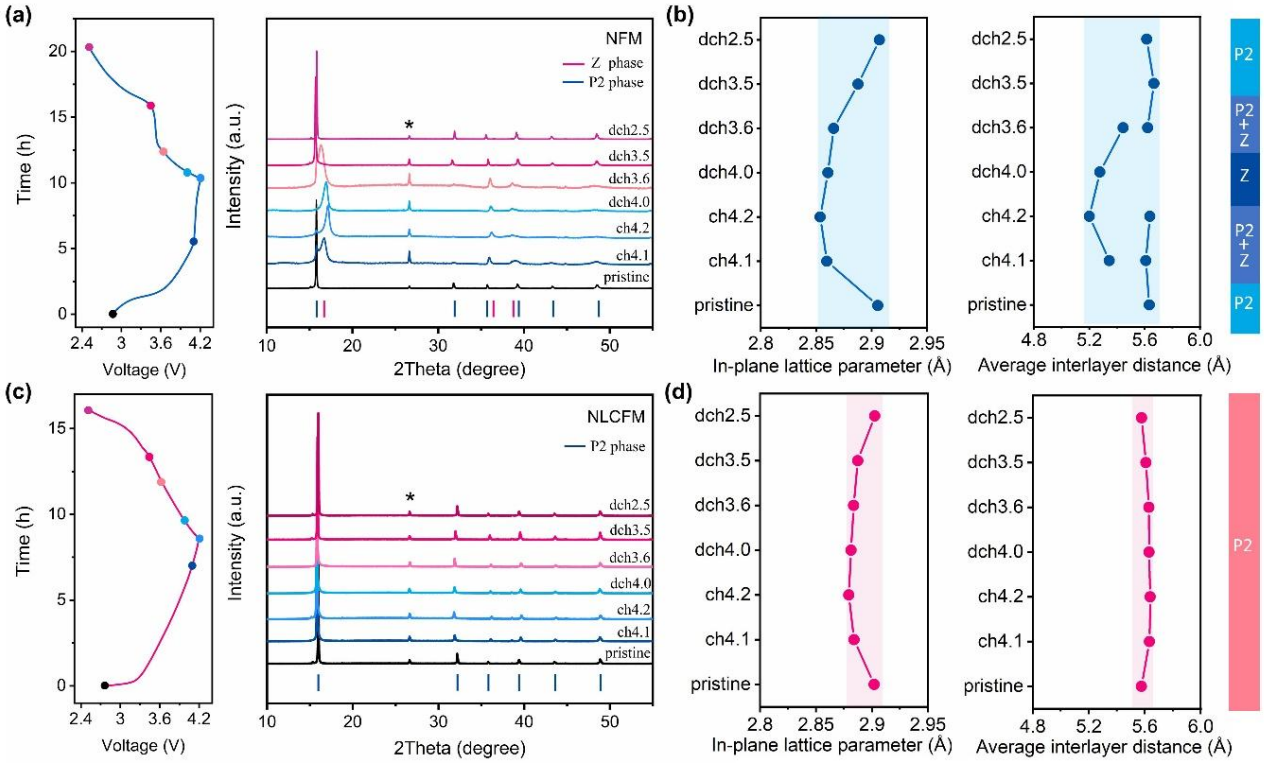

Fig. 3. Ex-situ XRD characterization on the structural evolution of NFM and NLCFM electrodes. (a, c) The ex-situ XRD patterns were collected during the first cycle under a current rate of 0.1C for NFM and NLCFM electrodes, with the corresponding first cycle electrochemical curves on the left. * represents the peaks from Al foil. (b, d) The evolution of in-plane lattice parameter, average interlayer distance fitted by ex-situ XRD patterns.

Very different from the NFM electrode, the XRD patterns for NLCFM in Fig. 3c show no new peaks beyond the P2 phase during the entire charge and discharge process. The complete solid-solution reaction is also reflected in the continuous change of the in-plane lattice parameter and the average interlayer distance (Fig. 3d). Note that the color-highlighted regions representing the range of parameters evolution in the NFM electrode (1.79% along a-axis and 7.68% along c-axis) is much larger than that in the NLCFM electrode (0.78% along a-axis and 1.12% along c-axis). The obvious difference in structural characteristics between two samples lead to different electrochemical behaviors, indicating that the suppression of P2-Z host rearrangement should account for the improved rate capability and cycling life. Further inspections on the XRD patterns of the mono-doped samples at the fully charged state (Fig. S12) also demonstrate a similar phenomenon, in reasonable agreement with their performance (Fig. S10).

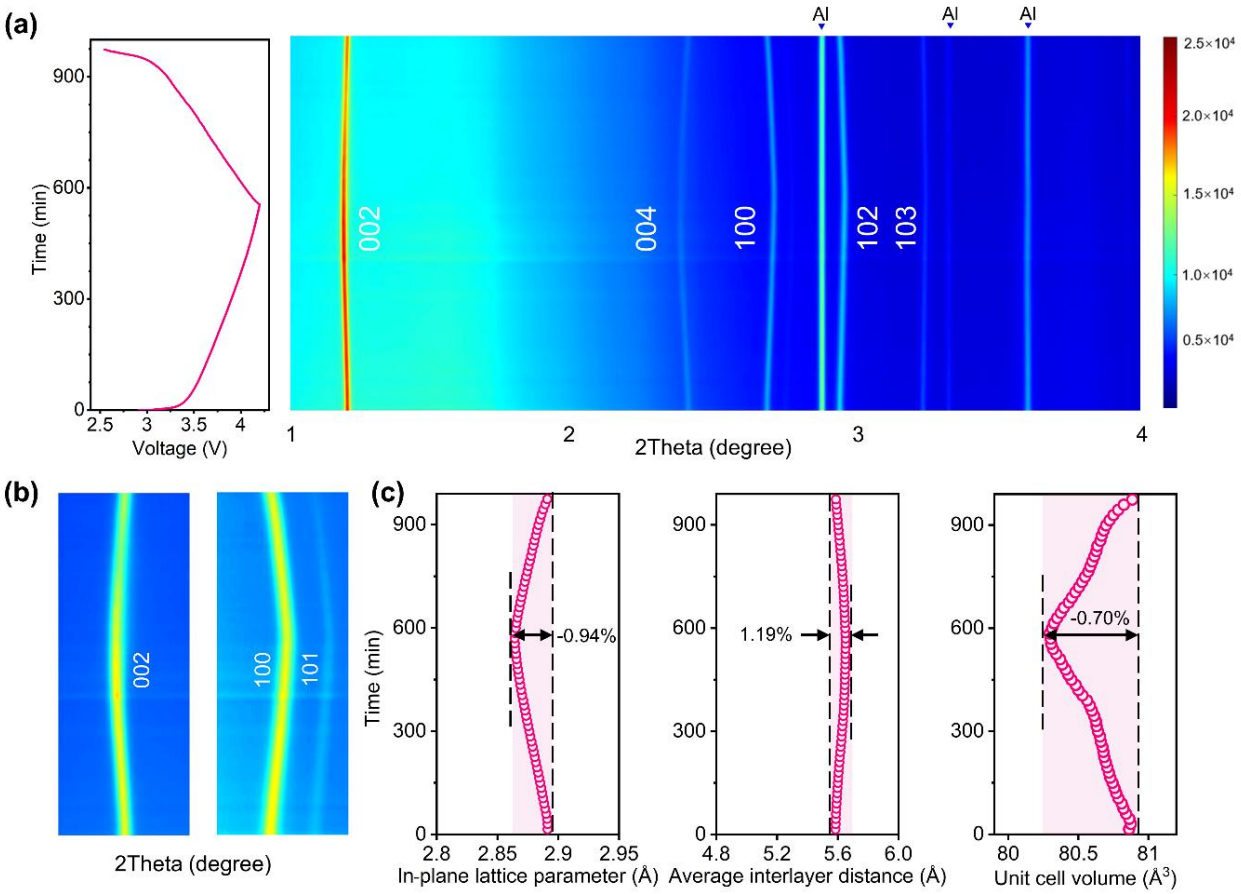

Fig. 4. In-situ synchrotron HEXRD characterization on the structural evolution of NLCFM electrode. (a) The contour plot of in-situ XRD patterns collected under a current rate of 0.1C, with the corresponding first cycle electrochemical curves on the left. (b)Processed images of Bragg peaks (002), (100) and (101) for NLCFM. (c) The evolution of in-plane lattice parameter, average interlayer distance and unit cell volume for the NLCFM electrode fitted by in-situ synchrotron XRD patterns.

For the NLCFM electrode, the single-phase solid-solution reaction with good reversibility is further confirmed by the in-situ HEXRD results (Fig. 4). Specifically, during the first charge, the (002) peak gradually shift leftward, while (100) and (101) peaks shift rightward, demonstrating the enlarged electrostatic repulsion between adjacent oxygen layers and electrochemical oxidation of TM ions respectively. Consequently, when Na^+ is extracted, nearly linear contraction of the in-plane lattice (0.93% along a-axis) and expansion of interlayer distance (1.19% along c-axis) were precisely monitored, showing a similar tendency with ex-situ XRD results. Not only could NLCFM electrode recover to pristine state regarding all the diffraction peaks and lattice parameters upon discharge, but it experiences an ultralow cell volume change of around 0.7% during the whole cycle. The nearly "zero strain" [46-48] performance represents the minimum value for the Li-doped P2 Fe/Mn-based and Cu-doped P2 Fe/Mn-based layered oxide cathodes for SIBs to date (Table S3). In short, ex-situ XRD and in-situ HEXRD corroboratively confirm that Li/Cu co-substitution for P2-type Fe- and Mn- based oxides can effectively prevent P2-Z phase transition and restrain the volume changes simultaneously during cycling, enabling the zero-strain characteristic and excellent electrochemical properties.

3.4. Failure analysis of electrodes

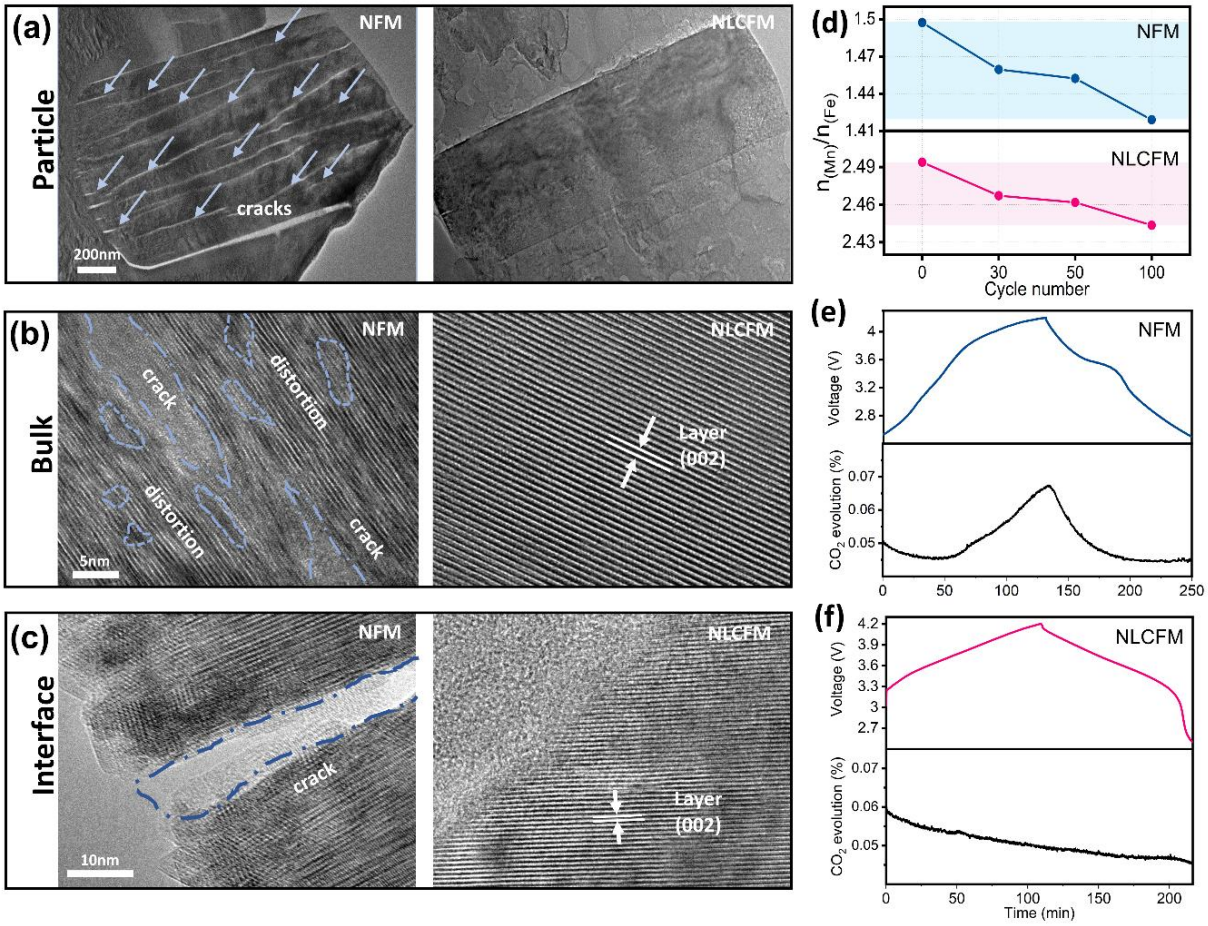

Fig. 5. Post-mortem analyses of NFM and NLCFM electrodes. (a) The cross-sectional images of the particles at low magnification. (b-c) The HRTEM images acquired in the bulk and at the interface. (d) The trend in the molar ratio of Mn to Fe within cathode electrodes during cycling. (e-f) CO_2 evolution of NFM and NLCFM cathodes upon first cycle.

In order to gain more insight into the differences between two materials in electrochemical reversibility, both of the electrodes after 50 cycles were subjected to post-mortem analysis. As shown in Fig. 5a, after cycling, a mass of cracks could be observed in the cross-sectional image of the NFM sample at low magnification. However, the NLCFM particle is almost intact and only a few tiny microcracks appear. At high magnification, the HRTEM patterns (Fig. 5b-c) acquired along the [100] axis show that distinct cracking and severe local structural distortion occurred in the bulk and surface region of the post cycled NFM, contrasting to the well-maintained (002) layered planes in Li/Cu co-substitution electrode. From these results, we found that the structural integrity of NFM and NLCFM are well in accordance with the cycling stability plots displayed in Fig.2, in which the NFM suffers rapid capacity fade while the NLCFM sample possesses extraordinary cyclability. It is also intriguing to note that the intragranular cracks (highlighted by dashed blue lines in Fig. 5b) exhibit evident crystallographic orientation, which is parallel to the (002) planes and consistent with the direction of Na^+ shuttling. Notably, similar intragranular cracking, which generally appears near the charging end with phase transition, has also been reported in other layered oxide cathodes for Na- and Li-ion batteries [49-52]. Therefore, combined with lattice parameter changes displayed in Fig. 3, cracks on the NFM particle can be correlated to the huge internal lattice stress caused by the deleterious P2-Z phase transition. Besides, with prolonged cycling, it is quite possible that the highly distorted lattice area shown in Fig.5b finally will evolve into cracking region.

In terms of the outermost section of cathodes particle (Fig. 5c), a thick degraded surface layer without the original ordered P2 lattice structure appeared in the NFM sample, which could be attributed to detrimental side reactions on the electrolyte-cathode interphase [53], including TM dissolution, electrolyte decomposition, etc. Particularly for the Mn-rich cathodes, Mn dissolution has been proven to be highly associated with surface degradation because of the destructive Jahn-Teller distortion and disproportionation of Mn^{3+} [54]. To verify this point, ICP-AES was employed to investigate the degrees of Mn dissolution from electrodes at different cycle rates. According to the profile in Fig. 5d, though both NFM and NLCFM electrodes show a decreasing trend in the mole ratio of Mn to Fe during half-cell cycling, the figure for NLCFM still exhibits fewer changes than NFM with the identical cycle period. By the end of 100 cycles, the figure for n(Mn)/n(Fe) has dropped from around 1.5 to below 1.42 in NFMO, while that of NLCFM decreased from nearly 2.5 to over 2.44, maintaining comparatively stable. Besides,

based on previous findings, Mn is more susceptible to the attack of HF and solvent molecules than Fe [39]. Hence, the above results clearly suggest that Mn dissolution in NLCFM is far less than NFM. This phenomenon could probably be explained by the minimization of the quantity of Mn^{3+} in NLCFM through Li/Cu co-substitution, which leads to low Mn^{3+}/Mn^{4+} redox activity (Fig. S8, 9), a corresponding decrease in Jahn-Teller distortion, disproportionation behavior, and consequent Mn dissolution [55, 56]. Meanwhile, as previously studied, the scavenging effect of Li dopant could also help to inhibit the TM cations dissolution and improve the interfacial stability [39]. Moreover, gas evolution, as another byproduct of the parasitic reactions (e.g., decomposition of the residual Na_2CO_3, electrolyte oxidation) on the cathode surface [57], was monitored by DEMS in the initial operation for the NFM and NLCFM cells. In Fig. 5e-f, the volume fraction of CO_2 evolution is plotted as a function of time. As a striking comparison, the CO_2 occurred at around 3.5V and peaked at the end of charging in the NFM cell, while there is no evidence of CO_2 release in the NLCFM cell, indicating a stable and clean electrode/electrolyte interface has been built for NLCFM, in keeping with the negligible surface structure collapse in NLCFM (Fig. 5c). All the above analyses clearly demonstrate that the repeated P2-Z phase transition with huge lattice strain directly induces cracking generation and particle disintegration, while both TM dissolution and interfacial side reactions contribute to severe capacity decay as well. In addition, during the following cycling, crack propagation and growth would inevitably result in more newly formed surfaces, and thus further accelerating electrolyte consumption, surface degradation, and resultant performance deterioration [50, 58].

To further evaluate the application prospects of materials, the NFM and NLCFM powders were either exposed to air or soaked into water, and then analyzed by XRD. As shown in Fig. S13, after aging experiments, the hydrated layered phase arises apparently in NFM samples, while the NLCFM powders show consistent XRD patterns compared with the pristine one. The excellent air-stability for NLCFM is attributable to the decreased distance of Na layers (Table. S2) and enhanced electrochemical redox potential (diluting redox couple of Mn^{3+}/Mn^{4+} and introducing Cu^{2+}/Cu^{3+}) [59, 60], which help to suppress the tendency toward Na^+ extraction and H_2O molecule insertion simultaneously.

4. Conclusion

In summary, a novel cathode material $Na_{0.65}Li_{0.08}Cu_{0.08}Fe_{0.24}Mn_{0.6}O_2$ for sodium-ion battery was designed and synthesized successfully, based on the Li/Cu co-substitution strategy of combining the strengths of different heteroatoms. It is confirmed the introduction of lithium and copper raises the average redox potential and stabilizes the lattice structure simultaneously. As a result, high average voltage of ~3.5V, high tolerance toward moisture, and the excellent cycle stability (88.2 % capacity retention after 500 cycles) are achieved, suggesting an extremely

promising cathode material. Combing with in-situ and ex-situ XRD characterizations as well as detailed post-mortem analysis, we revealed that stable host with less TM dissolution and negligible accumulated strains upon cycling is the key to deliver outstanding electrochemical performance. For the co-substituted electrode, the P2−Z phase transition is completely suppressed within the voltage range of 2.5−4.2 V, so achieving a solid-solution-like reaction and excellent cyclability. Such a universal co-substitution strategy could also be employed to other intercalation cathodes. Moreover, our findings demonstrate that realizing the complete solid-solution reaction during the Na^+ (de)intercalation is an instructive development direction for designing high-performance cathode materials for SIBs.

Declaration of competing interest

The authors declare no conflict of interest.

Acknowledgements

The research was financially supported by National Key R&D Program of China (2016YFB0700600 and 2020YFA0406203), National Natural Science Foundation of China (No. 52072008 and No. U2032167), Guangdong Basic and Applied Basic Research Foundation (Grant No. 2019A1515012060 and 2019B1515120028). This work gratefully acknowledges support from Clean Vehicles, US-China Clean Energy Research Centre (CERC-CVC2) under US DOE EERE Vehicle Technologies Office. This research used resources of the Advanced Photon Source (11-ID-C), a U.S. Department of Energy (DOE) Office of Science User Facility operated for the DOE Office of Science by Argonne National Laboratory under Contract No. DE-AC02-06CH11357.

References

[1] B. Dunn, H. Kamath, J.-M. Tarascon, Science 334 (2011) 928-935.

[2] C. Delmas, Adv. Energy Mater. 8 (2018).

[3] C. Vaalma, D. Buchholz, M. Weil, S. Passerini, Nat. Rev. Mater. 3 (2018) 18013.

[4] P.-F. Wang, Y. You, Y.-X. Yin, Y.-G. Guo, Adv. Energy Mater. 8 (2018).

[5] C. Delmas, C. Fouassier, P. Hagenmuller, Physica B+C 99 (1980) 81-85.

[6] Y. Sun, S. Guo, H. Zhou, Energy Environ. Sci. 12 (2019) 825-840.

[7] N. Yabuuchi, M. Kajiyama, J. Iwatate, H. Nishikawa, S. Hitomi, R. Okuyama, R. Usui, Y. Yamada, S. Komaba, Nat. Mater. 11 (2012) 512-517.

[8] M. Chen, Q. Liu, S.-W. Wang, E. Wang, X. Guo, S.-L. Chou, Adv. Energy Mater. 9 (2019).
[9] Y. Fang, Z. Chen, L. Xiao, X. Ai, Y. Cao, H. Yang, Small 14 (2018).
[10] X. Wang, S. Roy, Q. Shi, Y. Li, Y. Zhao, J. Zhang, J. Mater. Chem. A 9 (2021) 1938-1969.
[11] N. Yabuuchi, S. Komaba, Sci Technol Adv. Mater. 15 (2014) 043501.
[12] W.K. Pang, S. Kalluri, V.K. Peterson, N. Sharma, J. Kimpton, B. Johannessen, H.K. Liu, S.X. Dou, Z. Guo, Chem. Mater. 27 (2015) 3150-3158.
[13] W.M. Dose, N. Sharma, J.C. Pramudita, J.A. Kimpton, E. Gonzalo, M.H. Han, T. Rojo, Chem. Mater. 28 (2016) 6342-6354.
[14] B. Mortemard de Boisse, D. Carlier, M. Guignard, L. Bourgeois, C. Delmas, Inorg. Chem. 53 (2014) 11197-11205.
[15] V. Duffort, E. Talaie, R. Black, L.F. Nazar, Chem. Mater. 27 (2015) 2515-2524.
[16] H. Zhu, K.T. Lee, G.T. Hitz, X. Han, Y. Li, J. Wan, S. Lacey, A. Cresce, K. Xu, E. Wachsman, L. Hu, ACS Appl. Mater. Interfaces 6 (2014) 4242-4247.
[17] S. Kalluri, K.H. Seng, W.K. Pang, Z. Guo, Z. Chen, H.K. Liu, S.X. Dou, ACS Appl. Mater. Interfaces 6 (2014) 8953-8958.
[18] Z. Ding, Y. Liu, Q. Tang, Q. Jiang, J. Lu, Z. Xiao, P. Yao, M. Monasterio, J. Wu, X. Liu, Electrochim. Acta. 292 (2018) 871-878.
[19] L. Yang, X. Li, J. Liu, S. Xiong, X. Ma, P. Liu, J. Bai, W. Xu, Y. Tang, Y.-Y. Hu, M. Liu, H. Chen, J. Am. Chem. Soc. 141 (2019) 6680-6689.
[20] Y. Li, Z.-Y. Li, K. Sun, Y.-T. Liu, D.-F. Chen, S.-B. Han, L.-F. He, M.-J. Li, X.-L. Liu, M.-M. Wu, Ionics 26 (2019) 735-743.
[21] H. Wang, R. Gao, Z. Li, L. Sun, Z. Hu, X. Liu, Inorg. Chem. 57 (2018) 5249-5257.
[22] M. Huon Han, E. Gonzalo, N. Sharma, J. Miguel Lopez del Amo, M. Armand, M. Avdeev, J.J. Saiz Garitaonandia, T. Rojo, Chem. Mater. 28 (2016) 106-116.
[23] M. Zarrabeitia, E. Gonzalo, M. Pasqualini, M. Ciambezi, O. Lakuntza, F. Nobili, A. Trapananti, A. Di Cicco, G. Aquilanti, N.A. Katcho, J.M. López del Amo, J. Carrasco, M.Á. Muñoz-Márquez, T. Rojo, J. Mater. Chem. A 7 (2019) 14169-14179.
[24] D. Yuan, X. Hu, J. Qian, F. Pei, F. Wu, R. Mao, X. Ai, H. Yang, Y. Cao, Electrochim. Acta. 116 (2014) 300-305.
[25] L. Liu, X. Li, S.-H. Bo, Y. Wang, H. Chen, N. Twu, D. Wu, G. Ceder, Adv. Energy Mater. 5 (2015).
[26] Y.H. Jung, A.S. Christiansen, R.E. Johnsen, P. Norby, D.K. Kim, Adv. Funct. Mater. 25 (2015) 3227-3237.
[27] S. Xu, J. Wu, E. Hu, Q. Li, J. Zhang, Y. Wang, E. Stavitski, L. Jiang, X. Rong, X. Yu, W. Yang, X.-Q. Yang, L. Chen, Y.-S. Hu, J. Mater. Chem. A 6 (2018) 20795-20803.
[28] Q. Shen, X. Zhao, Y. Liu, Y. Li, J. Zhang, N. Zhang, C. Yang, J. Chen, Adv. Sci. (Weinh), 7 (2020) 2002199.
[29] U. Garg, W. Rexhausen, N. Smith, J. Harris, D. Qu, P. Guptasarma, J. Power Sources 431 (2019) 105-113.
[30] Y. Li, Z. Yang, S. Xu, L. Mu, L. Gu, Y.S. Hu, H. Li, L. Chen, Adv. Sci. (Weinh), 2 (2015) 1500031.

[31] D. Kundu, E. Talaie, V. Duffort, L.F. Nazar, Angew. Chem. Int. Ed. 54 (2015) 3431-3448.
[32] X. Gao, J. Chen, H. Liu, S. Yin, Y. Tian, X. Cao, G. Zou, H. Hou, W. Wei, L. Chen, X. Ji, Chem. Eng. J. 406 (2021).
[33] Y. Li, M. Chen, B. Liu, Y. Zhang, X. Liang, X. Xia, Adv. Energy Mater. 10 (2020).
[34] J. Deng, W.-B. Luo, X. Lu, Q. Yao, Z. Wang, H.-K. Liu, H. Zhou, S.-X. Dou, Adv. Energy Mater. 8 (2018).
[35] Y. Xiao, Y.-F. Zhu, H.-R. Yao, P.-F. Wang, X.-D. Zhang, H. Li, X. Yang, L. Gu, Y.-C. Li, T. Wang, Y.-X. Yin, X.-D. Guo, B.-H. Zhong, Y.-G. Guo, Adv. Energy Mater. 9 (2019) 1803978.
[36] C. Zhao, F. Ding, Y. Lu, L. Chen, Y.S. Hu, Angew. Chem. Int. Ed. 59 (2020) 264-269.
[37] J. Xu, D.H. Lee, R.J. Clément, X. Yu, M. Leskes, A.J. Pell, G. Pintacuda, X.-Q. Yang, C.P. Grey, Y.S. Meng, Chem. Mater. 26 (2014) 1260-1269.
[38] T. Jin, P.F. Wang, Q.C. Wang, K. Zhu, T. Deng, J. Zhang, W. Zhang, X.Q. Yang, L. Jiao, C. Wang, Angew. Chem. Int. Ed. 59 (2020) 14511-14516.
[39] Y. You, S. Xin, H.Y. Asl, W. Li, P.-F. Wang, Y.-G. Guo, A. Manthiram, Chem. 4 (2018) 2124-2139.
[40] C. Zhao, Z. Yao, Q. Wang, H. Li, J. Wang, M. Liu, S. Ganapathy, Y. Lu, J. Cabana, B. Li, X. Bai, A. Aspuru-Guzik, M. Wagemaker, L. Chen, Y.S. Hu, J. Am. Chem. Soc. 142 (2020) 5742-5750.
[41] C.W. Mason, F. Lange, K. Saravanan, F. Lin, D. Nordlund, ECS Electrochem. Lett. 4 (2015) A41-A44.
[42] Z. Yan, L. Tang, Y. Huang, W. Hua, Y. Wang, R. Liu, Q. Gu, S. Indris, S.L. Chou, Y. Huang, M. Wu, S.X. Dou, Angew. Chem. Int. Ed. 58 (2019) 1412-1416.
[43] X. Zheng, P. Li, H. Zhu, K. Rui, G. Zhao, J. Shu, X. Xu, W. Sun, S.X. Dou, Energy Storage Mater. 15 (2018) 257-265.
[44] E. Talaie, V. Duffort, H.L. Smith, B. Fultz, L.F. Nazar, Energy Environ. Sci. 8 (2015) 2512-2523.
[45] J.W. Somerville, A. Sobkowiak, N. Tapia-Ruiz, J. Billaud, J.G. Lozano, R.A. House, L.C. Gallington, T. Ericsson, L. Häggström, M.R. Roberts, U. Maitra, P.G. Bruce, Energy Environ. Sci. 12 (2019) 2223-2232.
[46] S. Guo, Y. Sun, P. Liu, J. Yi, P. He, X. Zhang, Y. Zhu, R. Senga, K. Suenaga, M. Chen, H. Zhou, Sci. Bull. 63 (2018) 376-384.
[47] Y. Cao, Q. Zhang, Y. Wei, Y. Guo, Z. Zhang, W. Huang, K. Yang, W. Chen, T. Zhai, H. Li, Y. Cui, Adv. Funct. Mater. 30 (2020) 1907023.
[48] Y. Wang, L. Wang, H. Zhu, J. Chu, Y. Fang, L. Wu, L. Huang, Y. Ren, C.J. Sun, Q. Liu, X. Ai, H. Yang, Y. Cao, Adv. Funct. Mater. 30 (2020).
[49] J. Xu, Z. Han, K. Jiang, P. Bai, Y. Liang, X. Zhang, P. Wang, S. Guo, H. Zhou, Small 16 (2020) e1904388.
[50] P. Yan, J. Zheng, M. Gu, J. Xiao, J.G. Zhang, C.M. Wang, Nat. Commun. 8 (2017) 14101.
[51] K. Wang, P. Yan, M. Sui, Nano Energy 54 (2018) 148-155.
[52] J. Song, K. Wang, J. Zheng, M.H. Engelhard, B. Xiao, E. Hu, Z. Zhu, C. Wang, M. Sui, Y. Lin, D. Reed, V.L. Sprenkle, P. Yan, X. Li, ACS Energy Lett. 5 (2020) 1718-1725.
[53] L.J. Krause, V.L. Chevrier, L.D. Jensen, T. Brandt, J. Electrochem. Soc. 164 (2017) A2527-A2533.

[54] T. Liu, A. Dai, J. Lu, Y. Yuan, Y. Xiao, L. Yu, M. Li, J. Gim, L. Ma, J. Liu, C. Zhan, L. Li, J. Zheng, Y. Ren, T. Wu, R. Shahbazian-Yassar, J. Wen, F. Pan, K. Amine, Nat. Commun. 10 (2019) 4721.

[55] J. Billaud, G. Singh, A.R. Armstrong, E. Gonzalo, V. Roddatis, M. Armand, T. Rojo, P.G. Bruce, Energy Environ. Sci. 7 (2014) 1387-1391.

[56] E. Gonzalo, N. Ortiz-Vitoriano, N.E. Drewett, B. Acebedo, J.M. López del Amo, F.J. Bonilla, T. Rojo, J. Power Sources 401 (2018) 117-125.

[57] J. Xia, R. Petibon, A. Xiao, W.M. Lamanna, J.R. Dahn, J. Power Sources 330 (2016) 175-185.

[58] K.-J. Park, J.-Y. Hwang, H.-H. Ryu, F. Maglia, S.-J. Kim, P. Lamp, C.S. Yoon, Y.-K. Sun, ACS Energy Lett. 4 (2019) 1394-1400.

[59] W. Zuo, J. Qiu, X. Liu, F. Ren, H. Liu, H. He, C. Luo, J. Li, G.F. Ortiz, H. Duan, J. Liu, M.-S. Wang, Y. Li, R. Fu, Y. Yang, Nat. Commun. 11 (2020).

[60] H.-R. Yao, P.-F. Wang, Y. Gong, J. Zhang, X. Yu, L. Gu, C. OuYang, Y.-X. Yin, E. Hu, X.-Q. Yang, E. Stavitski, Y.-G. Guo, L.-J. Wan, J. Am. Chem. Soc. 139 (2017) 8440-8443.

Supporting Information

A highly stable host with ultralow strain in a layered Fe/Mn-based cathode for advanced Sodium-ion Batteries

Rui Qi[a,1], Mihai Chu[a,1], Wenguang Zhao[a], Ziwei Chen[a], Lei Liao[b], Shisheng Zheng[a], Lei Xie[c], Tongchao Liu[d], Yang Ren[e], Lei Jin[f], Khalil Amine[d,g], Feng Pan[a,] and Yinguo Xiao[a,*]*

[a] School of Advanced Materials, Peking University, Shenzhen Graduate School, Shenzhen, 518055, China

[b] Beijing National Laboratory for Condensed Matter Physics, Institute of Physics, Chinese Academy of Sciences, 100190 Beijing, China

[c] Institute of Nuclear Physics and Chemistry, China Academy of Engineering Physics, Mianyang, 621900, China

[d] Chemical Sciences and Engineering Division, Argonne National Laboratory, Lemont, IL 60439, USA

[e] X-ray Science Division, Argonne National Laboratory, Lemont, IL 60439, USA

[f] Ernst Ruska-Centre for Microscopy and Spectroscopy with Electrons, Forschungszentrum Jülich GmbH, 52425 Jülich, Germany

[g] Material Science and Engineering, Stanford University, Stanford, CA 94305, USA

Author Information

1 These authors contributed equally to this work.

* Corresponding author: panfeng@pkusz.edu.cn (F. Pan), y.xiao@pku.edu.cn (Y. Xiao)

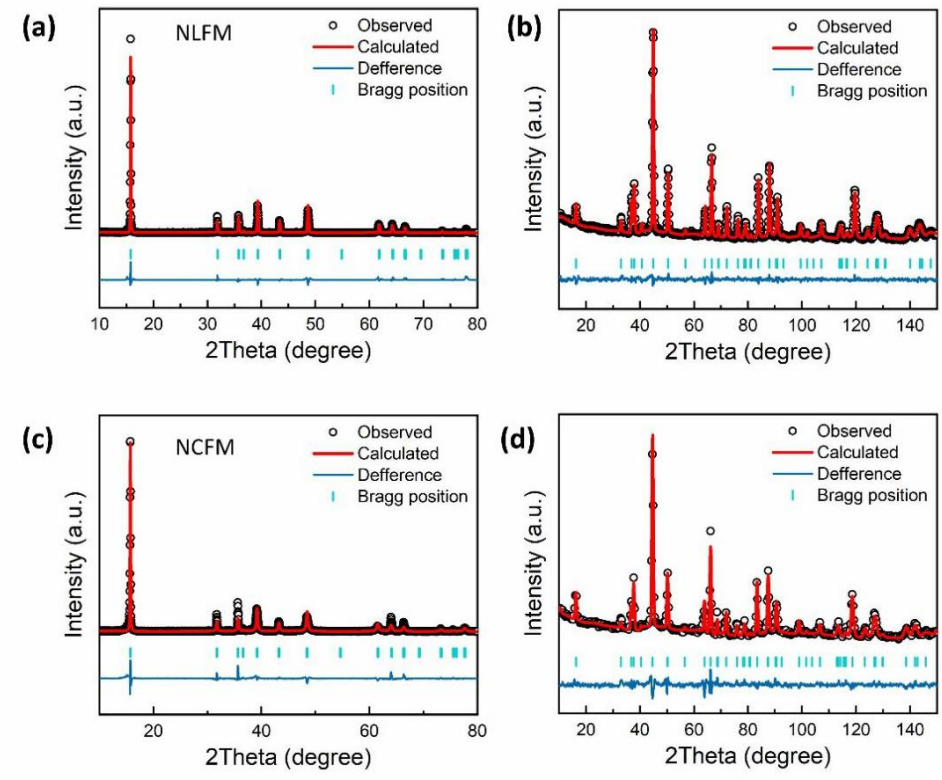

Fig. S1. Structural characterization on mono-doped samples. Observed and calculated XRD and NPD profiles for (a-b) NLFM and (c-d) NCFM: (black) observed; (red) calculated; (blue) difference plot; (green bars) Bragg reflections.

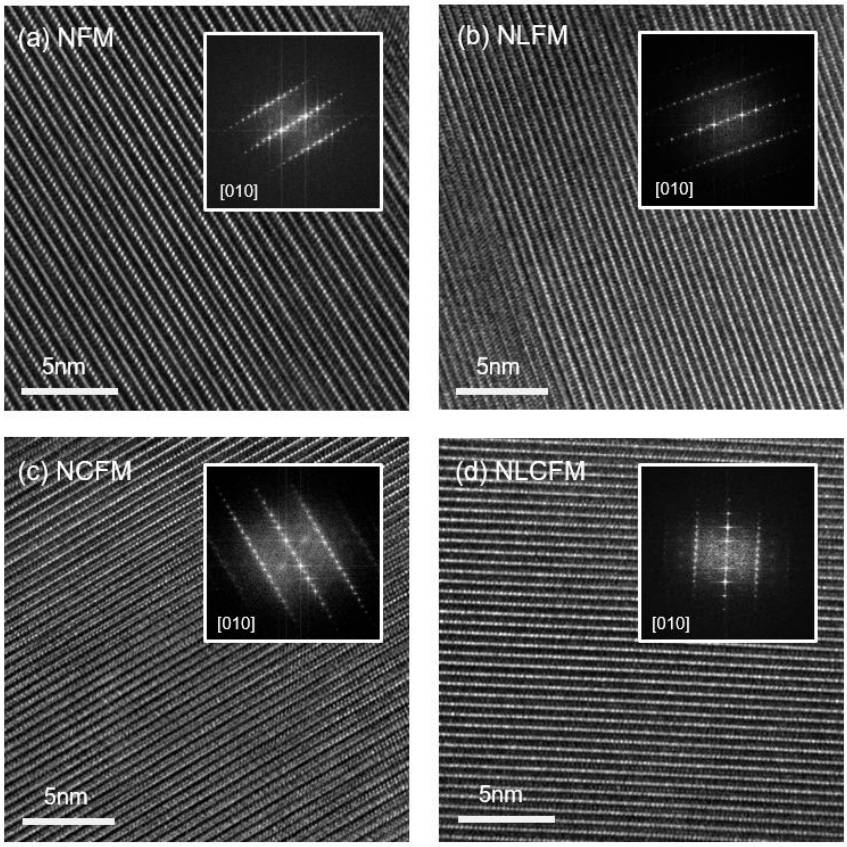

Fig. S2. High-resolution TEM images with insets of FFT images of as-synthesized samples.

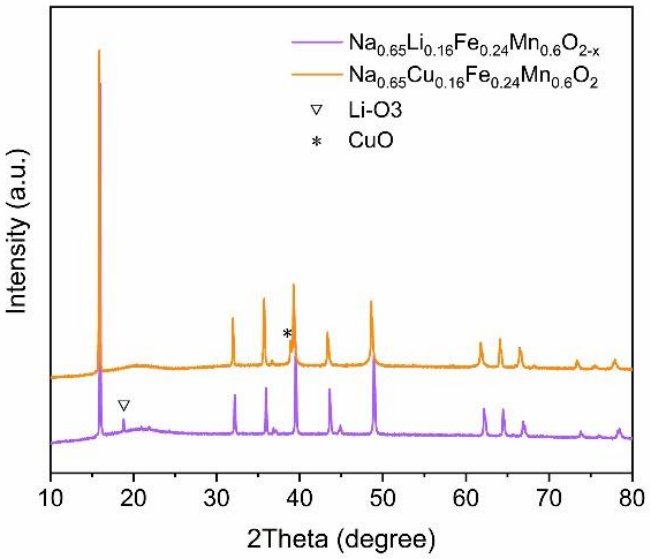

Fig. S3. XRD patterns of as-designed single-heteroatom-substituted samples (expected stoichiometry: Na: Li: Fe: Mn = 0.65: 0.16: 0.24: 0.6; Na: Cu: Fe: Mn = 0.65: 0.16: 0.24 :0.6).

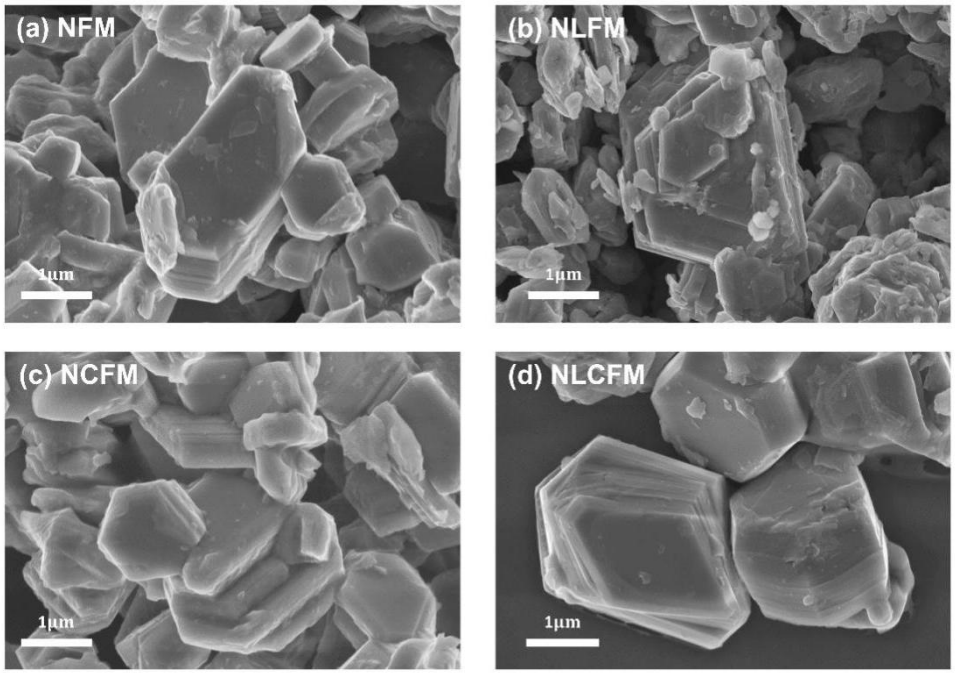

Fig. S4. SEM images of as-synthesized samples for (a) NFM, (b) NLFM, (c) NCFM and (d) NLCFM, respectively.

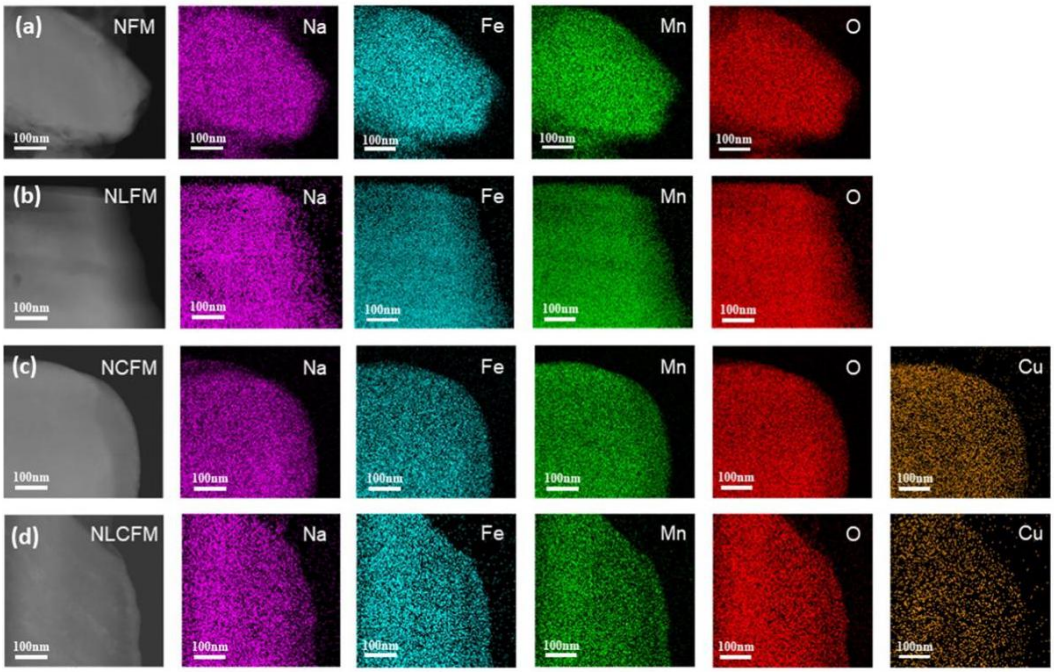

Fig. S5. SEM images of particles and corresponding EDS elemental mappings of Na, Fe, Mn, O and Cu for (a) NFM, (b) NLFM, (c) NCFM, and (d) NLCFM, respectively.

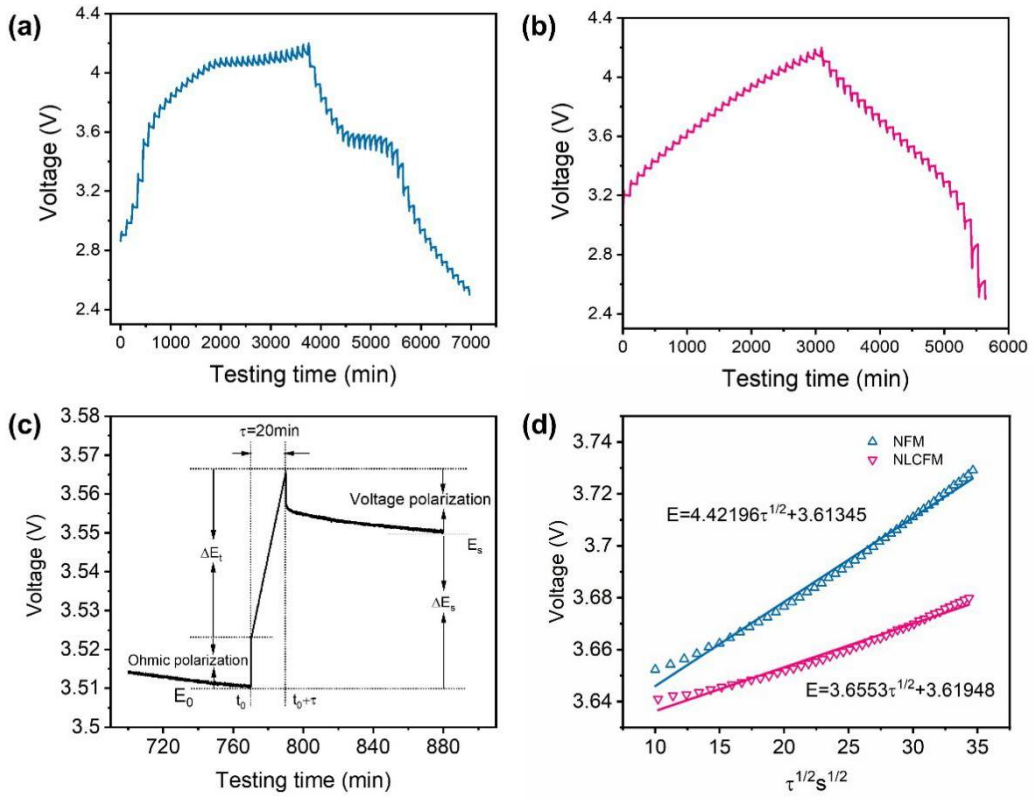

Fig. S6. Kinetic characteristics for NFM and NLCFM electrodes. GITT profiles for initial cycle of (a) NFM and (b) NLCFM electrode in the voltage window of 2.5-4.2 V. (c) Current vs. cell potential for a single titration step in GITT. (d) Linear fit of the cell potential vs. the square root of time ($\tau^{1/2}$) with different pulse currents.

Because the cell voltage as a function of $\tau^{1/2}$ shows a linear relationship, the chemical diffusion coefficient D_{Na^+} can be obtained from the formula:

$$D_{Na^+} = \frac{4}{\pi}\left(\frac{m_B V_m}{M_B S}\right)^2 \left(\frac{\Delta E_S}{\Delta E_\tau}\right)^2, \qquad (\tau \ll \frac{L^2}{D_{Li^+}})$$

m_B , V_m, and M_B are the actual mass, the molar volume, and the molar mass of the cathode materials, respectively, while τ is the constant current pulse time and S is the contact area between the electrode and electrolyte (here, the geometric surface of the electrode). ΔE_S and ΔE_τ are marked in the Fig. S4c.

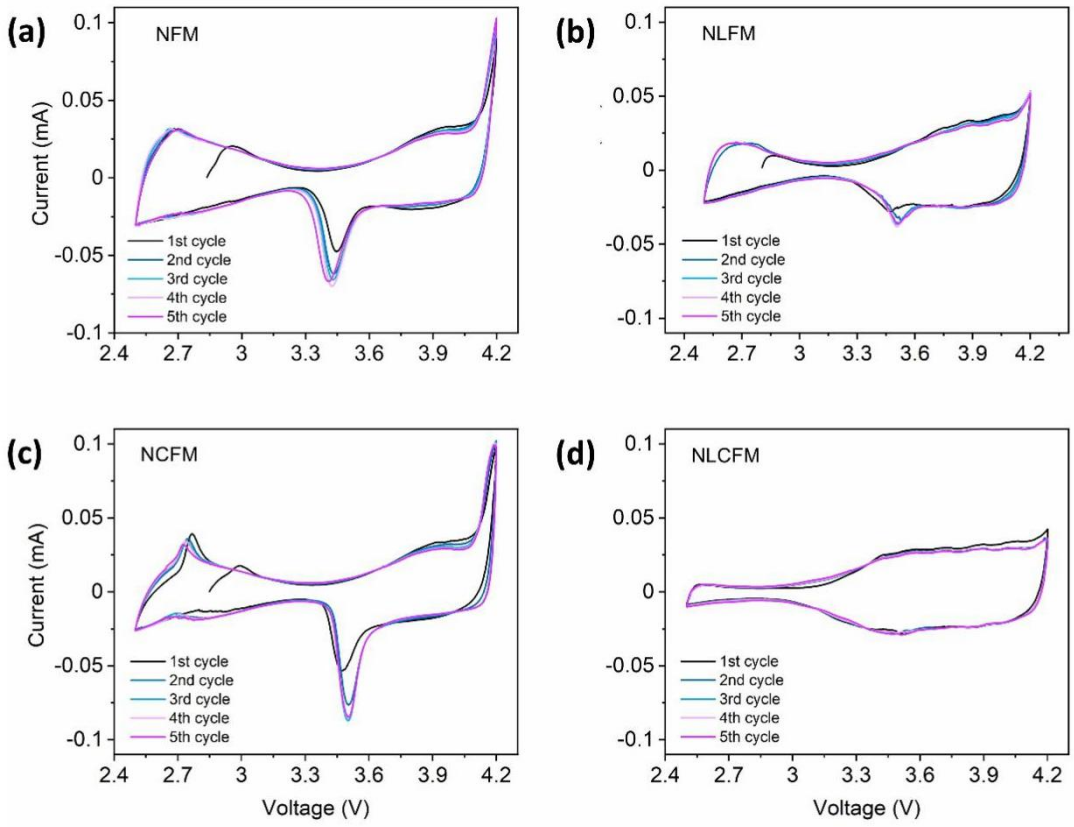

Fig. S7. Cyclic voltammogram curves of (a) NFM, (b) NLFM, (c) NCFM and (d) NLCFM electrodes between 2.5-4.2 V at 0.1 mV s^{-1} scan rate for 5 cycles.

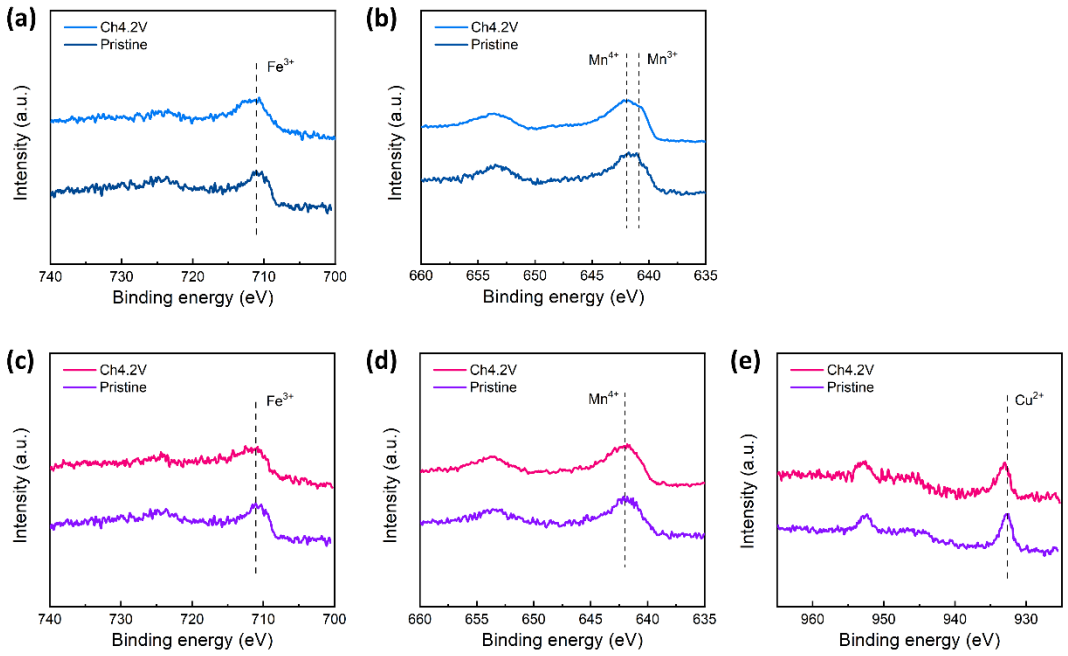

Fig. S8. XPS spectra of Mn 2p, Fe 2p and Cu 2p before and after charged to 4.2V for (a-b) NFM and (c-e) NLCFM electrodes.

For the NFM electrode, the binding energies of Fe $2p_{3/2}$ and Mn $2p_{3/2}$ are 711.3 eV and 641.7 eV, respectively, corresponding to the Fe^{3+}, mixed Mn^{3+} and Mn^{4+}, while for NLCFM electrode the binding energies of Fe $2p_{3/2}$, Mn $2p_{3/2}$ and Cu $2p_{3/2}$ are 711.3 eV, 642.2 eV, and 933.2 eV, respectively, corresponding to the Cu^{2+}, Fe^{3+} and Mn^{4+}. Given the previous ICP-AES results (Table S1), the formulas could be denoted as $Na_{0.65}Fe^{3+}_{0.4}Mn^{3+}_{0.25}Mn^{4+}_{0.35}O_2$ and $Na_{0.65}Li^{+}_{0.08}Cu^{2+}_{0.08}Fe^{3+}_{0.24}Mn^{4+}_{0.6}O_2$.

As a result, when the NFM electrode is charged to 4.2V, the binding energies of Fe and Mn shift to higher values, suggesting the oxidations of Fe^{3+} to Fe^{4+}, and Mn^{3+} to Mn^{4+}.When the NLCFM electrode is charged to 4.2V, the peaks of Cu 2p and Fe 2p both move to higher binding energy while the peaks of Mn 2p almost do not shift, indicating that redox couples of Fe and Cu are both active and almost provide all capacity upon initial charge process. These changes are in accordance with our original intention, the proportion of trivalent Mn is greatly reduced after the co-substitution of monovalent Li ions and bivalent Cu ions.

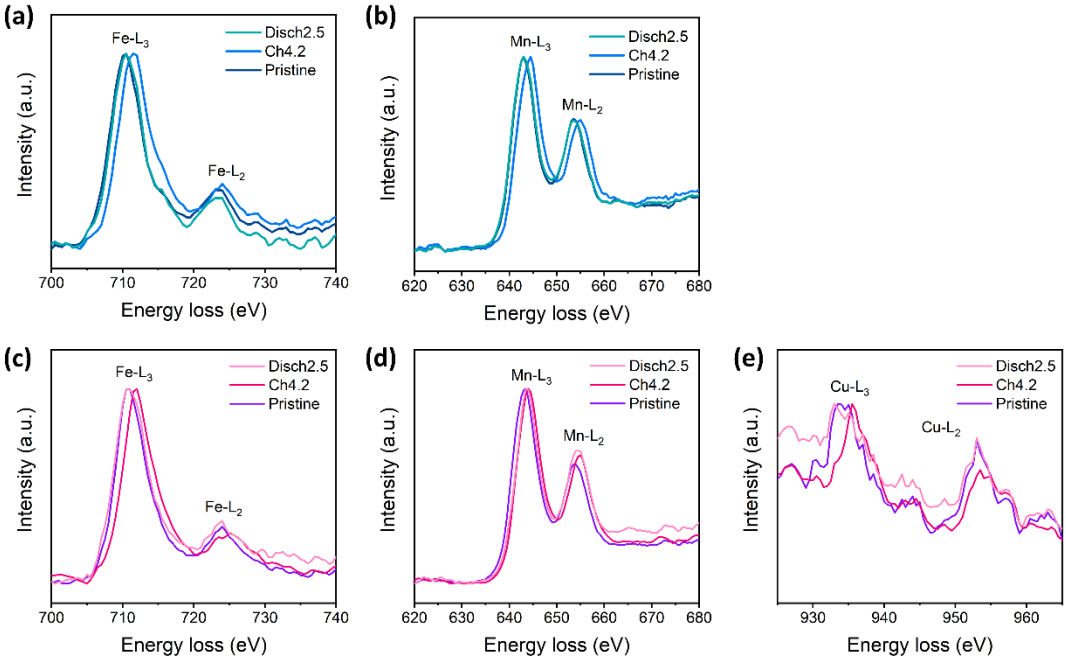

Fig. S9. EELS spectra of Mn 2p, Fe 2p and Cu 2p at different charged/discharged states during the 1st cycle for (a-b) NFM and (c-e) NLCFM electrodes.

The charge compensation mechanism is further supported by the EELS results. In the case of the NFM electrode, when fully charged to 4.2V, the EELS spectra of Fe $L_{2,3}$, Mn $L_{2,3}$ move to higher energy values with 1 and 1.5 eV shifts respectively, which confirm the oxidation of Fe^{3+} and Mn^{3+}.

For NLCFM electrode, the peaks of Fe $L_{2,3}$ and Cu $L_{2,3}$ at the fully charged state both move to higher energy values, while the peaks of Mn $L_{2,3}$ barely shift all the time.

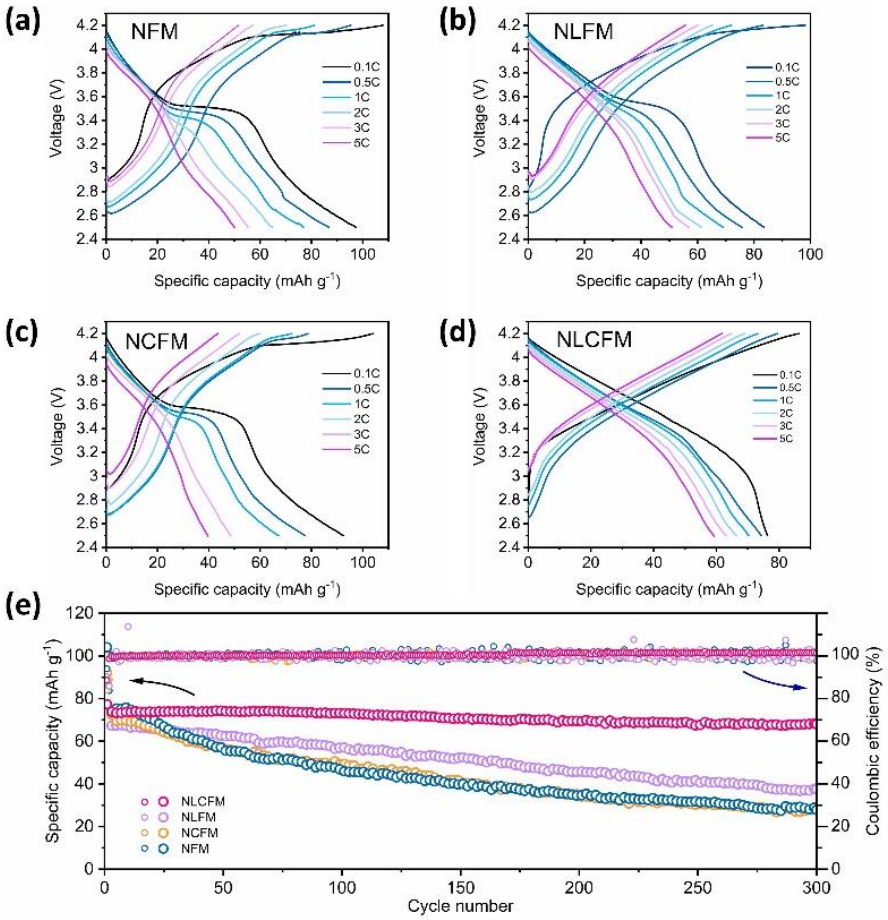

Fig. S10. The electrochemical performance of four as-prepared electrodes. The charge/discharge curves at different rates for (a) NFM, (b) NLFM, (c) NCFM and (d) NLCFM electrodes. (e) Cycling performance of four as-prepared electrodes at 2C over 300 cycles.

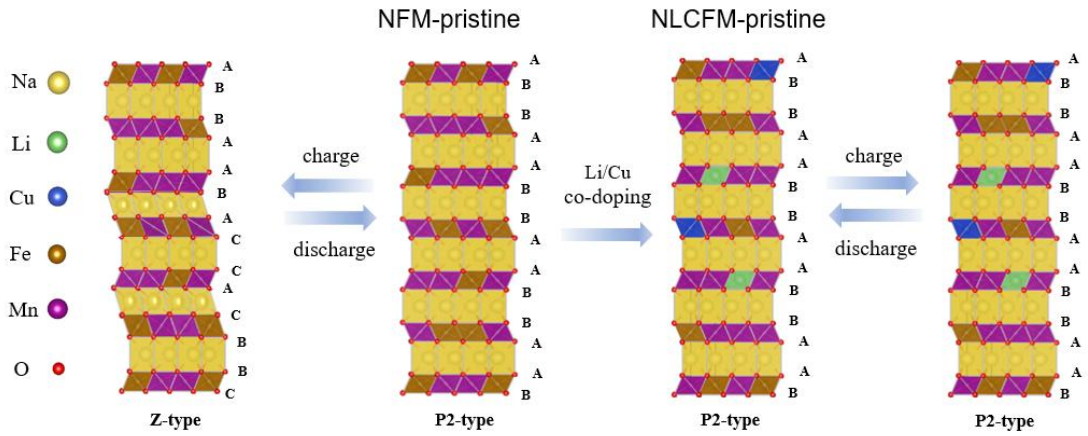

Fig. S11. Schematic illustration of the phase evolution of NFM and NLCFM electrodes.

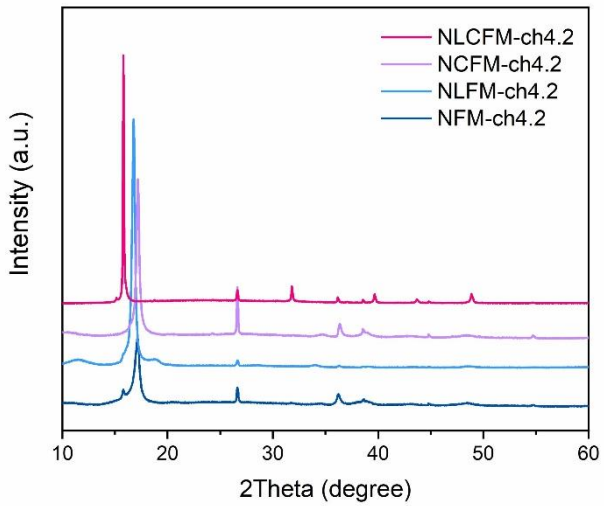

Fig. S12. Ex-situ XRD results for four electrodes at fully charged state.

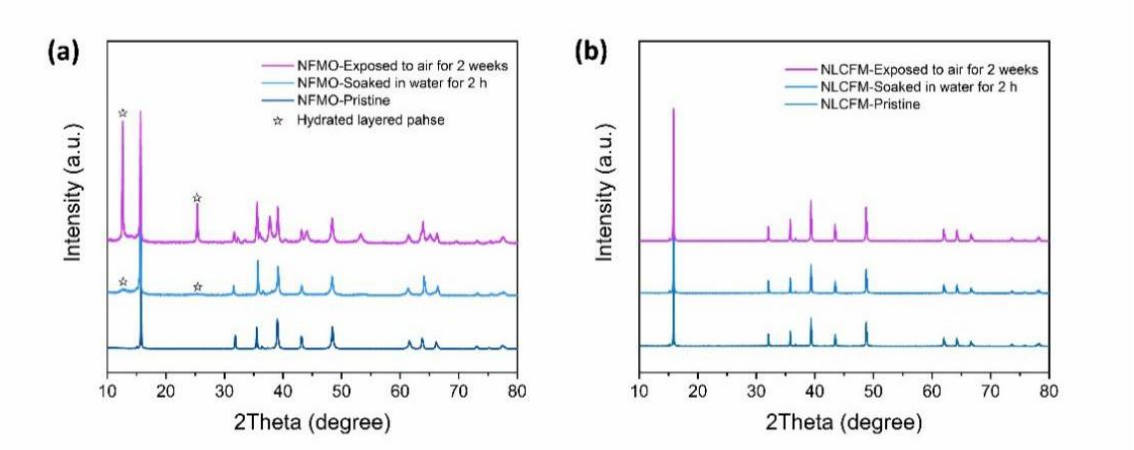

Fig. S13.The result of aging experiments for (a) NFM and (b) NLCFM powder samples.

Table S1. Chemical compositions of NFM, NLFM, NCFM, and NLCFM determined by ICP-AES measurements.

Sample	Theoretical molar ratio of Na: Fe: Mn: Li: Cu	Na: Fe: Mn: Li: Cu by ICP-AES
NFM	0.65: 0.40: 0.60: 0: 0	0.642: 0.405: 0.602: 0: 0
NLFM	0.65: 0.32: 0.60: 0.08: 0	0.647: 0.323: 0.606: 0.078: 0
NCFM	0.65: 0.32: 0.60: 0: 0.08	0.644: 0.318: 0.603: 0: 0.084
NLCFM	0.65: 0.24: 0.60: 0.08: 0.08	0.652: 0.239: 0.598: 0.082: 0.077

Table S2. The refined structural information of the as-prepared samples.

Sample	NFM	NLFM	NCFM	NLCFM
a (Å)	2.92237	2.90046	2.91495	2.90275
b (Å)	2.92237	2.90046	2.91495	2.90275
c (Å)	11.23363	11.20496	11.23364	11.14693
V ($Å^3$)	83.0848	81.6345	82.6634	81.3401
$T_{(Na)}$	3.57499	3.54861	3.57724	3.51864
$T_{(TM)}$	2.04182	2.05387	2.03958	2.05483
O_z	0.09088	0.09165	0.09078	0.09217
R_{exp}	2.39	2.44	2.32	2.68
R_p	3.05	2.78	2.81	3.54
R_{wp}	3.88	3.49	3.73	4.51
χ^2	2.64	2.04	2.60	2.83

Table S3. Comparison of the volume change in this work with those previously reported for the P2-type Cu- or Li-doped Fe/Mn-based layered oxides for sodium-ion battery.

Sample	Volume Change	Voltage Change	Reference
$Na_{0.66}Li_{0.18}Fe_{0.12}Mn_{0.7}O_2$	3.5%	1.5-4.5V	J. Am. Chem. Soc. 2019, 141, 6680−6689
$Na_{7/9}Cu_{2/9}Fe_{1/9}Mn_{2/3}O_2$	1.32%	2.5-4.2V	Adv. Sci. 2015, 2, 1500031
$Na_{0.7}Cu_{0.2}Fe_{0.2}Mn_{0.6}O_2$	0.08%	2.5-4.2V	J. Mater. Chem. A, 2018, 6, 20795
$Na_{0.76}Cu_{0.22}Fe_{0.30}Mn_{0.48}O_2$	1.43%	2.0-4.0V	Adv. Sci. 2020, 7, 2002199